Unveiling 3D Morphology of Multiscale Micro-Nano Silver Sintering for Advanced Electronics Manufacturing by Ptychographic X-ray Nano-Tomography

Yu-Chung Lin[1#], Xiaoyang Liu[1#], Kang-Wei Chou[2], Esther H. R. Tsai[3,5], Chonghang Zhao[1], Mirko Holler[3], Ana Diaz[3], Stanislas Petrash*[2], Yu-chen Karen Chen-Wiegart*[1,4]

1 Department of Materials Science and Chemical Engineering, Stony Brook University, Stony Brook, NY, 11794, USA
2 Henkel Corporation, Bridgewater, NJ, 08807, USA
3 Paul Scherrer Institut, Forschungsstrasse 111, CH-5232 Villigen, Switzerland
4 National Synchrotron Light Source - II, Brookhaven National Laboratory, Upton, NY, 11973, USA
5 Center for Functional Nanomaterials, Brookhaven National Laboratory, Upton, NY 11973, USA

*Corresponding Authors: karen.chen-wiegart@stonybrook.edu, stan.petrash@henkel.com
[#] Joint first authors

Abstract

This work investigated the sintering processing-structure-property relationship of a multi-scale silver materials: micro-particles with nano-features, particularly on their three-dimensional (3D) morphology. The target application is to replace conventional lead-based solders in advanced electronic manufacturing. Unlike lead-based solders, silver powders are suited to satisfy increasingly demanding mechanical, electrical and thermal requirements, meanwhile being free of health effect. Sintering the material at a low temperature and without applied pressure are desirable conditions, which resulted in a preferred use of silver nanoparticles, as nano-features have higher driving force to sinter with the decrease in particle size. However, nano-sized ~~silver~~ powders present potential health/environmental effects. To address the trade-off between the benefits and shortcomings of nano- vs micro-particles, this work studied a novel multi-scale silver paste, namely micron-sized powders with nano-sized features. To get quantitative 3D visualization of micro- and nano-scale features, we applied Ptychographic X-ray Computed Nano-Tomography. we established correlations between conditions (thermal aging, pressure, substrate metallization), mechanical properties (adhesive peel force) and morphological parameters (feature size, constituent volume ratio, surface curvature, 3D microstructures). Using novel 3D X-ray nano-imaging technique, we demonstrated one can design multiscale materials while balancing complex demands required in advanced electronics manufacturing and research directions in materials design and characterization.

1. Introduction

Advanced materials design and processing plays a critical role in electronics manufacturing, with electronics packaging being one of the key areas. A common method of component attachment in electronics industry is using lead (Pb)-based eutectic alloys for binding adjacent layers together to form three-dimensional (3D) architectures. However, there are many environmental, health and regulatory challenges are associated with using Pb-based alloys in advanced electronics and beyond[1]. Some lead-free alternatives such as Zn-, Au- or Bi-based alloys have disadvantages including poor solderability, weak corrosion resistance and causing damages in devices[2, 3]. Therefore, there has been growing fundamental, multidisciplinary research effort is to design new lead-free materials for effective interfacial joining, driven by the need to develop the next generation electronics packaging and processing strategies.

Silver (Ag) paste which is based on sintering micron- and nano-scale Ag powder became an attractive potential alternative, because Ag paste has been shown to bond and cure at a relatively low temperature, 200-300 $^{\circ}$C[4, 5]. Sintering is a process that joins interfaces of materials by various diffusion routes at a temperature that is sufficiently high to allow diffusion to occur, but yet below the material's melting point of the sintering materials[6]. The operating temperature, which is lower than the melting point of the joining materials, enables creating joints by sintering Ag particles without generating liquid phases. This has a great advantage as it eliminates the re-solidification procedure in the process, which is highly complex and can generate secondary phases via kinetic-limited processes, which are challenging to control precisely.

The conventional Ag sintering process involves pressure-assisted sintering of micron-scale powders[7-9], driving up the processing constraints and cost. Developing a pressure-less Ag sintering process was thus inspired, where the use of micron-sized metallic particles with nano-sized features plays a key role in removing the required pressure in materials processing. The

presence of nano-sized features resulted in a higher surface area per volume thus the intrinsic sintering driving force becomes higher, lowering the required processing temperature and pressure. Furthermore, sintering Ag particles with relatively small size in one dimension provide enhanced properties including good shear strength and electric conductivities[10]. On the other hand, the particles are still micron-sized in other two dimensions, which avoids the toxicity issues associated with nanoparticles.

Prior studies focused on characterizing the mechanical properties including shear or tensile stress of the sintered Ag with different sintering time, pressure, temperature and aging time using X-ray diffraction, scanning electron microscopy and X-ray tomography[11, 12]. X.Milhet et al.[13] studied micron Ag paste and quantitatively analyzed the connectivity, pore geometry, pore spatial distribution and density evolution with different aging temperature of the porous sintered Ag to study the growth, Oswald ripening and clustering of the pores using *in situ* X-ray tomography. Suzuki *et al.*[14], used finite element analysis (FEA) to simulate the mechanical behavior based on 3D microstructures obtained from serial focused ion beam – scanning electron microscopy (FIB-SEM) cross-sectional images. In addition, the substrate and die metallization were correlated with the mechanical properties, microstructural characterization and long-term reliability. Chua et al. studied the direct bond copper (DBC) substrate without metallization and observed the formation of an additional layer of copper (Cu) oxide[15]. Other research studied the influence of different metallization layers such as PdAg, Au and Ag, which generally exhibited good initial mechanical properties, *i.e.* die shear test values above 15 MPa. However, after sintering, only the Ag metallization sample conformed to the required die shear test values[15, 16]. For gold (Au) metallization layer, the changes in morphology and interface included voids formation or a depletion layer would weaken the mechanical properties[17, 18]. While prior characterization on these structures provided valuable information, further analysis in 3D to visualize the interfaces and the layer-to-layer interaction is required to further understand the processing-structure-property of this multi-layer structure[19].

Ptychographic X-ray computed tomography (PXCT)[20, 21] is a novel high-resolution 3D microscopy method. As a lensless coherent imaging method, the resolution of PXCT is not limited by the X-ray optics and the reconstructed images directly and quantitatively represent the 3D distribution of the electron density of the structure. Applications of PXCT have been demonstrated in various important fields including biomedicine to quantify detailed structures within a bone [19] and electronics[22] to reveal the finest details of a computer chip. In this work, PXCT was applied to study a novel sintered Ag made of micron-sized metallic particles with nano-sized features which play a key role in pressure-less sintering during materials processing. Furthermore, the interface between sintered Ag, substrate and metallization layer were visualized by PXCT with quantitative 3D electron-density mapping. Specifically, the effects of Au metallization, sintering pressure and post-processing thermal aging on the 3D morphological parameters were investigated in conjunction with the die attachment mechanical properties. The critical 3D morphological parameters were quantified, including the feature size distribution of the different phases and spatially resolved porosity as a function of metallization substrates, sintering pressure and thermal aging conditions and curvature distribution of Ag surface. Overall the work provides an understanding of the formation of important features including porosity gradient, voids and depletion layers at different layers and sheds the light on understanding micro-nano materials, electronics and thin films for the processing-structure-property correlation utilizing PXCT.

2. Results and Discussion

The sintering and aging conditions are summarized in Table 1, which are chosen to be consistent with processing parameters used in electronics die attach applications as well as in relevant studies[13, 23] (see supplementary material for detailed sample preparation). The effects of different conditions - pressure, aging and metallization – on the 3D morphology were

investigated, with a focus on the 3D morphology at the interface between nano-Ag sintered powder and the substrate interface. Figure 1 shows the 3D segmented and cropped reconstructions of PXCT and the corresponding cross-sectional view of the segmented volumes. Different colors represent different phases as labeled in Figure 1. The effects of different controlled parameters including Au metallization, aging, and pressure are discussed below.

The effect of Au metallization can be seen by comparing Figure 1 (A) (sample A without Au metallization) and Figure 1 (B) (sample B with Au metallization). In sample B, the Au metallization layer shown in yellow between the DBC substrate and sintered Ag layer shown in grey appeared to act as a passivation layer to prevent the oxygen from diffusing through the porous Ag to react with the DBC substrate. This is evident from the fact that without such Au metallization on the substrate, sample A forms an additional phase shown as green at the interface of Ag and DBC substrate.

This phase is clearly visible in Figure 2, which shows X-ray projection images collected from the same Sample A measured by ptychography and X-ray fluorescence. This phase was previously identified to be of Cu oxide using energy-dispersive electron spectroscopy (EDS). It showed that aging a similar sintered Ag sample without metallization layer at 300°C in air will expose the sample in rich oxygen environment, leading to the formation of a thick Cu oxide layer[24, 25]. Literature also showed that the Cu oxide can further inter-diffuse with the Ag phase after thermal annealing under 300 $^{\circ}$C for 50 hours. This Cu oxide - Ag inter-diffusion leads to an interconnected 'interlock' structure between the Cu substrate and Ag phases, therefore results in a better adhesion of Ag to the substrate. The enhancement of the adhesion is evident from Figure 3, which shows better adhesion values for Cu substrate (~1 N/mm) versus Au-metallized substrate (~0.5 N/mm)[15]. However, after a long-term aging, the thickness of the Cu oxide layer tends to increase, and the joint will become weaker, due to the mismatch of the thermal expansion coefficients between Cu, Cu oxide, and sintered Ag.

Aged at 250°C for 24 hours, sample B formed a denser Ag layer with lower porosity (shown as grey, indicated with red arrows) when contacting with Au layer (shown as yellow) as shown in Figure 1 (B); this layer also showed interdiffusion between Ag and Au. Right above the denser Ag layer, a layer with higher porosity (shown in black, indicated with green arrows) was also identified. In contrast, without the thermal aging (sample C) the density of porous Ag structure was distributed uniformly, without forming a denser layer at the interface with the Au metallization (Figure 1 C). Muralidharan *et al.* found that a similar sample aged at 300 °C for 24 hours formed a void-free layer with adjacent 'depletion' layer and the growth of the thickness of this void-free layer was reported to be proportional to the aging time[26]. Meanwhile, the depletion layer with higher porosity was found to gradually increase with increased aging time. The formation of this depletion layer with higher porosity is consistent with Kirkendall effect. This phenomenon had been reported in diffusion couple of Ag-Au alloys at 875°C[27-29], caused by the different diffusivities between Ag and Au in their inter-diffusion. Such depletion layer near the interface can potentially harm the mechanical properties of the materials. Chen *et al.* found that the VFL and depletion layer were not seen after 1000 hours of aging at 300°C[24]. However, aging the sample for 24 hours is not long enough to eliminate the depletion layer, thus both the depletion and void free layer were found in sample B.

Application of pressure during sintering appears to have a significant effect on 3D morphology of sintered Ag. Comparison between Figure 1 C (sample C with pressure) and Figure 1 D (sample D without pressure) showed much larger interconnects in Ag network for the sample sintered with no pressure. The pressure-sintered sample showed considerably smaller pore size, but with thinner sample interconnections. As a result, if pressure is applied during sintering of Ag powders, the adhesion is significantly reduced (Figure 3). Two effects can contribute to this result: First, the larger Ag ligament interconnects and pore sizes in sample D could be largely due to the higher sintering time needed for pressure-less sintering condition. Second, the pressure may disrupt the "stacking' of the flat Ag particles. This particle 'stacking' appears to

be responsible for thicker interconnects in sample C, while in sample D, the pressure applied during sintering appears to disrupt the stacking arrangement resulting in finer structure with thinner interconnects.

The phase distribution profiles of pore, Ni, Ag, Au, Cu and Cu oxide for each of the samples correlated with the interface morphology are shown in Figure 4. The distance was measured relative to the Ag substrate interface. The data provides quantitative information about the 3D sample morphology, and a more accurate representation of the sample, as compared to information obtained from analysis of 2D cross-section obtained by the FIB-SEM technique.

Figure 4 (A-B) showed that in sample A without Au layer, Cu oxide (shown in green) formed and diffused into the Ag layer (shown by the green line). Because Cu oxide is an insulator, the electrical conductivity of the materials would be reduced. In contrast, in Sample B which had an Au metallization layer given by the magenta line in Figure 4 (C), no Cu oxide was formed at the interface because Au metallization and Ni layer prevented the formation of Cu oxide. Moreover, in Figure 4 (C), the phase volume fraction of Ag and Au increased together indicating that the Ag-Au interdiffusion (indicated by black arrows) occurred at the interface where the Au and Ag layers were directly in contact. Above the Ag-Au interdiffusion layer, the Ag phase volume fraction decreased from ∼ 70% to ∼ 50% and the porosity increased from ∼25% to ∼ 50% which indicate the formation of a 'depletion layer' of Ag. This phenomenon may be caused by that the diffusivity of Ag was higher than Au; as a result, the Ag diffused faster to the Au metallization layer, creating voids formed by Kirkendall Effect[30, 31]. This increased porosity at the interface is visualized in Figure 4 (D).

Figure 4 (E-F) show the phase volume fraction profiles of each elements and a direct visualization at the interface of Sample C (Au-P-nA). Compared to Sample B which was measured after an aging process, the Au profile in Sample C is compact and obvious as shown quantitatively in Figure 4 (E) and Sample C had a denser and distinct Au layer as visualized in

Figure 4 (F); this indicates that Au and Ag did not inter-diffuse during the sintering process and the interdiffusion between Ag and Au in Sample B was a result of the aging process. In addition, Sample C showed a relatively uniform distribution of porosity (~ 40%) throughout the Ag layer. Hence, sintering process did not promote the inter-diffusion between Au and Ag, but aging process will decrease the long-term stability and reduce the Ag adhesion to the Au-metallized substrate by forming pores at the interface between Au and Ag (Figure 3).

The effect of applied pressure during sintering process has been studied by comparing Sample C (with pressure) and D (without pressure) as shown in Figure 4 (G-H). For Sample D, a longer sintering time was necessary to ensure structural integrity as the sintering was conducted without applied pressure; as a result, the coarsening of the structure was observed driven by minimizing the surface energy in porous media. At the interface, since the sintering time is much longer than Sample C, the Ag would migrate to the Au layer. The depletion layer was formed after sintering process where the volume fraction of Ag decreased, and porosity increased.

The quantitative analysis of pore and Ag size distribution of samples with different control parameters is shown in Figure 5 (A). Sample A without Au layer had a pore size similar to sample B with Au layer. However, the Ag feature size of sample B was much smaller than that of sample A. The results indicated that the Au layer can hinder the migration between the sintered Ag and Cu and lead to the uniform structure of Ag size. In addition, the Ag feature size distribution in sample A was much broader than that of sample B. Furthermore, comparing to sample D (Au-nP-nA) when sintering without the pressure, the Au layer still cannot prevent Ag and pore growth.

The Ag size distribution did not show significant differences in samples with and without aging conditions between sample B and sample C. The pore size of sample B was larger than that of sample C due to aging effect. The pore size distribution of sample B showed a broader

distribution compared to sample C. Under pressure-assisted sintering condition with Au layer, aging would affect the width of pore size distribution but not the size of Ag as shown in samples B and C. The aging also affected the migration of Ag that caused a depletion zone with high porosity in the middle of the Ag layer as in sample B.

Without pressure-assisted sintering, the sample D showed both broader Ag and pore size distribution, with larger average Ag and pore size. However, for sample C with 5 min pressure sintering process, the Ag and pore size were much smaller than that of sample D. Pressure-assisted sintering was not ideal in IC manufacturing, and this study indicated that for this particular Ag pressure-less sintering created larger interconnects (Figure 1). This is consistent with the longer time that is required to sinter the sample without the applied pressure. According to the previous study, when sintering for a longer time, the diffusion of the Ag would lead to coarsening and densification of Ag[32].

It is known that the different curvatures in 3D structure lead to a chemical potential difference, which drives mass transportation and morphological evolution, including sintering. Hence, studying the curvature difference at the interface is important. Figure 5 (B-D) shows the histogram of mean (H) and Gaussian (K) surface curvature on Ag phase and correlated 3D visualization of different samples. Comparing the mean curvature of sample A and B, both of them showed that the majority were negative meaning that the surface of Ag had more concave points with lower chemical potential. But the mean curvature of sample B with Au metallization showed a narrower distribution with Full Width Half Maximum (FWHM) at 0.00789 nm^{-1} (Table S1); in addition, both mean and Gaussian curvature distributions were closer to 0 meaning that the surface shape of sample B with Au metallization contains more plane-like or saddle-point-like features. This type of structure would be closer to equilibrium, with less tendency to further evolve, likely caused by the densification process.

The mean and Gaussian curvatures of sample B and C were compared to study the influence of aging. The FWHM of the mean curvature in sample B was 0.00789 nm^{-1}, which was smaller than that of Sample C at 0.00822 nm^{-1} (Table S1). Hence, sample B with aging presented a narrower mean curvature range, which means that the aging process further smoothed the surface of Ag particles. Lastly, when sintering with pressure, as was done in sample C, the driving force included external stress and intrinsic curvature-driven stress. Comparing Sample C and D, sample C with pressure had lower average (-0.00245 nm^{-1}) and median (-7E-07 nm^{-1}) value of mean curvature with more concavities at the Ag surface.

3. Conclusion

We studied the 3D morphology for nano-Ag sintering process with controlled parameters: presence or absence of pressure during sintering, aging, and substrate metallization. A quantitative 3D morphological analysis was conducted, including the determination of the material phase profile in the direction perpendicular to the interface, calculation of feature size distribution, and 3D volume rendering. The 3D volume rendering showed that the sample without Au metallization formed an additional phase of Cu oxide. The samples with aging condition or pressure-less sintering (sintering for longer duration) exhibited a void-free layer right at the Au/Ag interface, followed by an Ag depletion layer. The sample with pressure-assisted sintering, Au metallization, and without aging showed a uniform density profile of sintered Ag. Qualitatively, this sample showed both smaller pore and sintered Ag cluster size, as compared to the sample sintered without pressure, with Au surface metallization and without aging. Moreover, in the analysis of phase distribution profile and feature size distribution, we quantified the joints interface properties and the morphological feature at the interface. Lastly, the curvature analysis of the Ag surface indicated the influence of control parameters on the chemical potential, which affected the kinetics of sintering process.

The results indicated that the pressure-less sintering without Au metallization of the interface provides the best initial quality of Ag film in the initial state. Somewhat surprisingly, thermal aging did not increase the overall numerical density of Ag film. Instead, the Ag and Au inter-diffused and formed a depletion layer, likely contributing to a weaker adhesion strength.

In this research, synchrotron ptychographic X-ray computed tomography (PXCT) provided the detailed and quantitative information of 3D microstructure to demonstrate the joints interface properties in aging, Au metallization, and pressure parameter. The work shed light on the mechanisms of potential degradation mechanisms in sintered Ag powders for die attachment. The promise of using PXCT as an advanced 3D imaging tool for examining new materials in semiconductor design and processing was also demonstrated. Furthermore, the electrical conductivity of the materials after sintering and aging process is of great interest for future research.

4. Experimental Section

Four samples were prepared for the high-resolution PXCT measurements. For sample A without an Au metallization layer, Ag powders (Henkel Belgium N. V) were printed on the DBC substrate with a total thickness of 75 μm. A 1.8×1.8 cm^2 die was attached on the Ag layer for further sintering process by annealing. For the remaining three samples, a nickel (Ni) metallization layer was firstly printed on the DBC substrates, then the Au metallization layer was applied prior to the Ag layer (Figure 6 C). The pristine nano-Ag powder and sintered nano-Ag structure are shown in Figure 6 (A-B). The samples were milled into a cylinder with diameter 14-16 μm by FIB followed by a lift-out process[33] (Figure 6 B) and were finally placed on a special sample mount[34] for PXCT measurements[20, 35], which were performed at the cSAXS beamline (X12SA, Figure 6 D) at the Swiss Light Source, Paul Scherrer Institute (see supplementary material for experiment)[22]. After collecting the data, the central region in each

of the 3D reconstruction image stack was cropped for further analysis. Different materials in the sample were then segmented based on their density difference shown in the grayscale histogram, using Avizo software (FEI, Ver. 9.4, see supplementary material for detailed segmentation and quantification process). The phases include Cu, Cu oxide, Ni, Au, Ag and pore (air). The adhesion test was conducted by performing 90° peel test. The peel speed of 8 mm/sec was used for samples.

SUPPLEMENTARY MATERIAL

See supplementary material for sintering and aging process for samples, PXCT experiment, data analysis process and quantification of mean curvature.

Reference

[1]   W. J. Plumbridge, R. J. Matela, A. Westwater, *Structural integrity and reliability in electronics : enhancing performance in a lead-free environment*, Kluwer Academic Publishers, Dordrecht ; Boston **2003**.

[2]   G. S. Jeong, D. H. Baek, H. C. Jung, J. H. Song, J. H. Moon, S. W. Hong, I. Y. Kim, S. H. Lee, Nat. Commun. **2012**, *3*.

[3]   C. Chen, H. M. Tong, K. N. Tu, Annu. Rev. Mater. Res. **2010**, *40*, 531.

[4]   E. Ide, S. Angata, A. Hirose, K. F. Kobayashi, Acta Mater. **2005**, *53*, 2385.

[5]   A. Hu, J. Y. Guo, H. Alarifi, G. Patane, Y. Zhou, G. Compagnini, C. X. Xu, Appl. Phys. Lett. **2010**, *97*.

[6]   S. M. A. Robert W. Balluffi, W. Craig Carter, *Kinetics of Materials*, **2005**.

[7]   T. Wang, X. Chen, G. Q. Lu, G. Y. Lei, J. Electron. Mater. **2007**, *36*, 1333.

[8]   K. S. Siow, J. Alloys Compd. **2012**, *514*, 6.

[9]   Y. H. Mei, G. Chen, Y. J. Cao, X. Li, D. Han, X. Chen, J. Electron. Mater. **2013**, *42*, 1209.

[10] M. Y. Li, Y. Xiao, Z. H. Zhang, J. Yu, ACS Appl. Mater. Interfaces **2015**, *7*, 9157.

[11] P. Gadaud, V. Caccuri, D. Bertheau, J. Carr, X. Milhet, Mater. Sci. Eng., A **2016**, *669*, 379.

[12] X. M. James Carr, Pascal Gadaud, Severine A.E. Boyer, George E. Thompson, Peter Lee, J. Mater. Process. Technol. **2015**, 19.

[13] X. Milhet, A. Nait-Ali, D. Tandiang, Y. J. Liu, D. Van Campen, V. Caccuri, M. Legros, Acta Mater. **2018**, *156*, 310.

[14] T. Suzuki, T. Terasaki, Y. Kawana, D. Ishikawa, M. Nishimura, H. Nakako, K. Kurafuchi, IEEE Trans. Device Mater. Reliab. **2016**, *16*, 588.

[15] S. T. Chua, K. S. Siow, J. Alloys Compd. **2016**, *687*, 486.

[16] F. Yu, J. Z. Cui, Z. M. Zhou, K. Fang, R. W. Johnson, M. C. Hamilton, IEEE Trans. Power Electron. **2017**, *32*, 7083.

[17] F. a. J. R. a. H. M. Yu, Additional Conferences (Device Packaging, HiTEC, HiTEN, & CICMT) **2014**, *2014*.

[18] S. Seal, M. D. Glover, H. A. Mantooth, Ieee, "*Nanosilver Preform Assisted Die Attach for High Temperature Applications*", presented at *30th Annual IEEE Applied Power Electronics Conference and Exposition (APEC)*, Charlotte, NC, Mar 15-19, **2015**.

[19] M. Dierolf, A. Menzel, P. Thibault, P. Schneider, C. M. Kewish, R. Wepf, O. Bunk, F. Pfeiffer, Nature **2010**, *467*, 436.

[20] M. Holler, A. Diaz, M. Guizar-Sicairos, P. Karvinen, E. Farm, E. Harkonen, M. Ritala, A. Menzel, J. Raabe, O. Bunk, Sci. Rep. **2014**, *4*, 3857.

[21] A. Diaz, P. Trtik, M. Guizar-Sicairos, A. Menzel, P. Thibault, O. Bunk, Phys. Rev. B **2012**, *85*, 020104(R).

[22] M. Holler, M. Guizar-Sicairos, E. H. R. Tsai, R. Dinapoli, E. Muller, O. Bunk, J. Raabe, G. Aeppli, Nature **2017**, *543*, 402.

[23] K. S. Siow, J. Electron. Mater. **2014**, *43*, 947.

[24] S. Sakamoto, S. Nagao, K. Suganuma, J. Mater. Sci.: Mater. Electron. **2013**, *24*, 2593.

[25] H. J. Lee, J. Yu, J. Electron. Mater. **2008**, *37*, 1102.

[26] G. Muralidharan, D. N. Leonard, H. M. Meyer, J. Electron. Mater. **2017**, *46*, 4085.

[27] W. C. Mallard, R. F. Bass, L. M. Slifkin, A. B. Gardner, Phys. Rev. B **1963**, *129*, 617.

[28] O. Kubaschewski, Trans. Faraday Soc. **1950**, *46*, 713.

[29] M. H. Greene, A. P. Batra, R. C. Lowell, R. O. Meyer, L. M. Slifkin, Phys. Status Solidi A **1971**, *5*, 365.

[30] E. Gonzalez, J. Arbiol, V. F. Puntes, Science **2011**, *334*, 1377.

[31] R. O. Meyer, Bull. Am. Phys. Soc. **1969**, *14*, 389.

[32] C. Kittel, *Introduction to solid state physics*, Wiley, Hoboken, NJ **2005**.

[33] Y. C. K. Chen-Wiegart, F. E. Camino, J. Wang, ChemPhysChem **2014**, *15*, 1587.

[34] M. Holler, J. Raabe, R. Wepf, S. H. Shahmoradian, A. Diaz, B. Sarafimov, T. Lachat, H. Walther, M. Vitins, Rev. Sci. Instrum. **2017**, *88*, 113701.

[35] M. Holler, J. Raabe, A. Diaz, M. Guizar-Sicairos, C. Quitmann, A. Menzel, O. Bunk, Rev. Sci. Instrum. **2012**, *83*, 073703.

Sample	Metallization	Sintering Condition		Aging Temp. and Time	Abbreviation
		Sintering Pressure and Time	Sintering Temp. and Time		
A	No	10 MPa, 5 minutes	250 °C, 5 min	24 hr, 250 °C	nAu-P-A
B	Au	10 MPa, 5 minutes	250 °C, 5 min	24 hr, 250 °C	Au-P-A
C	Au	10 MPa, 5 minutes	250 °C, 5 min	No	Au-P-nA
D	Au	No	250 °C, 60 min	No	Au-nP-nA

Table 1 Sample preparation parameters to study the effects of the Au metallization, sintering conditions and aging condition in the 3D morphology of nano-silvers used in die attachments.
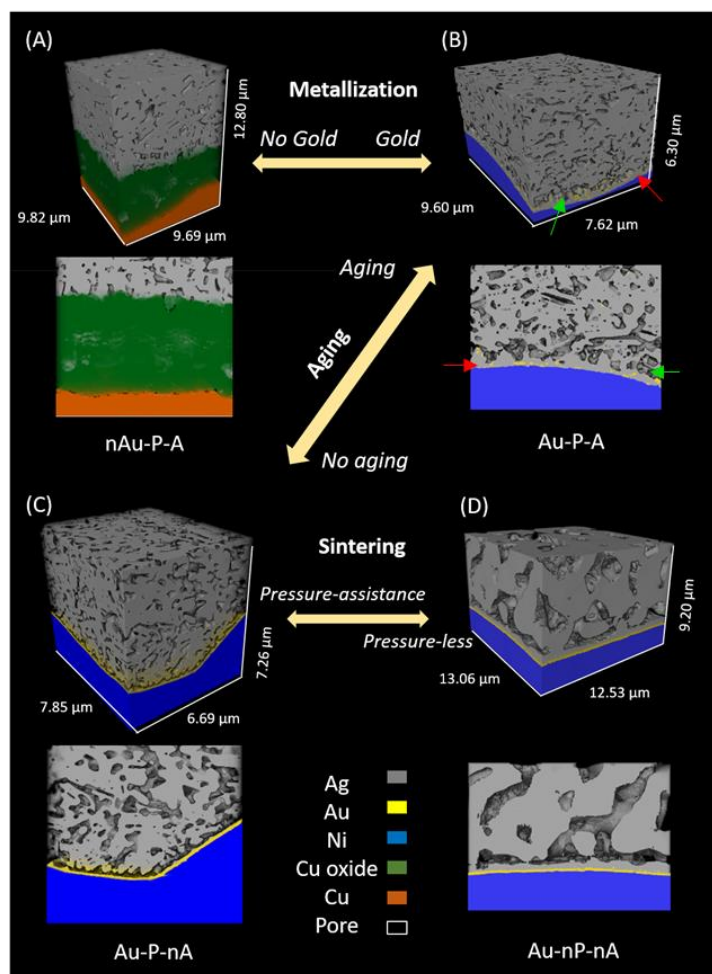
Figure 1 3D segmented reconstructions of sintered samples by ptychographic X-ray computed tomography (PXCT) showing phase structure: (A) Sample A: nAu-P-A (B) Sample B Au-P-A (C) Sample C: Au-P-nA, and (D) Sample D: Au-nP-nA; red arrows indicate a dense Ag layer and green arrows indicate a region higher porosity as a result of Au metallization layer. The opacity of the Cu oxide phase was altered for visualization. Videos of the samples can be viewed in Supporting Information.
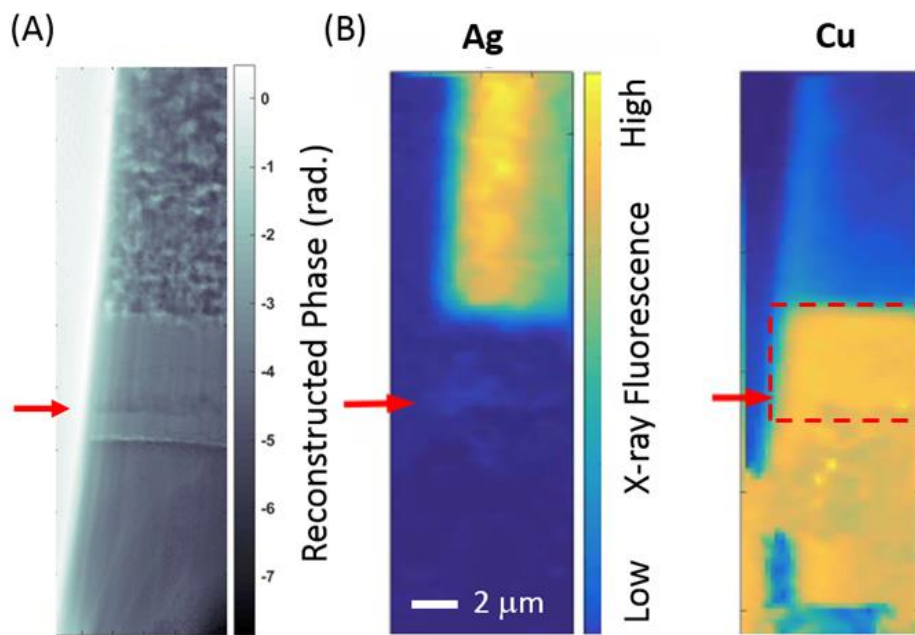
Figure 2 X-ray projection images collected from sample A. The same vertical location is shown with a red arrow as a guide for the eye. (A) Ptychographic projection of a region of interest within the sample. (B) Ag and (C) Cu X-ray fluorescence images of the same region, showing an interdiffusion Cu-rich layer (dashed frame) due to the lack of Au- layer. Some additional Cu signals were observed on the exterior region, likely due to the background signals of the sample mount.
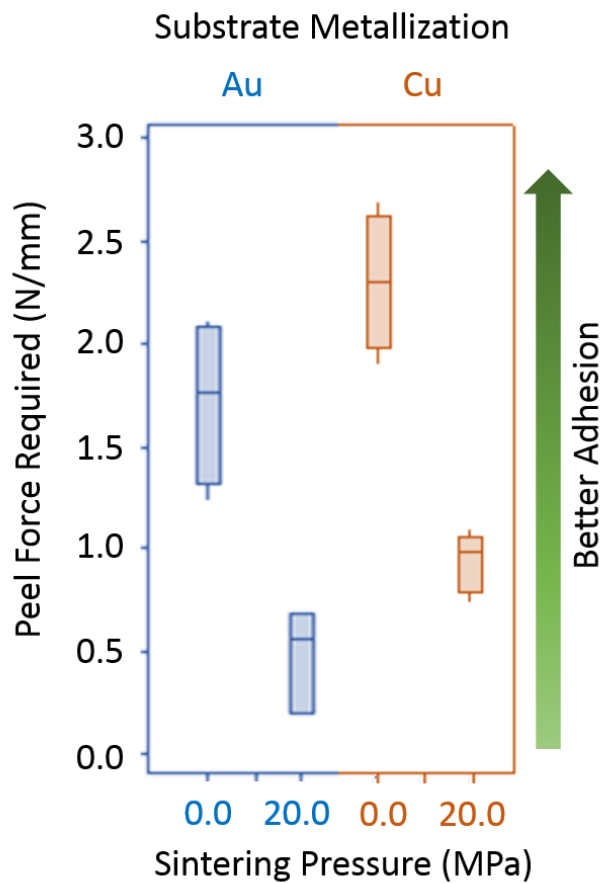
Figure 3 Peel data (in N/mm) on sintered Ag samples, showing the effect of substrate metallization and sintering pressure.
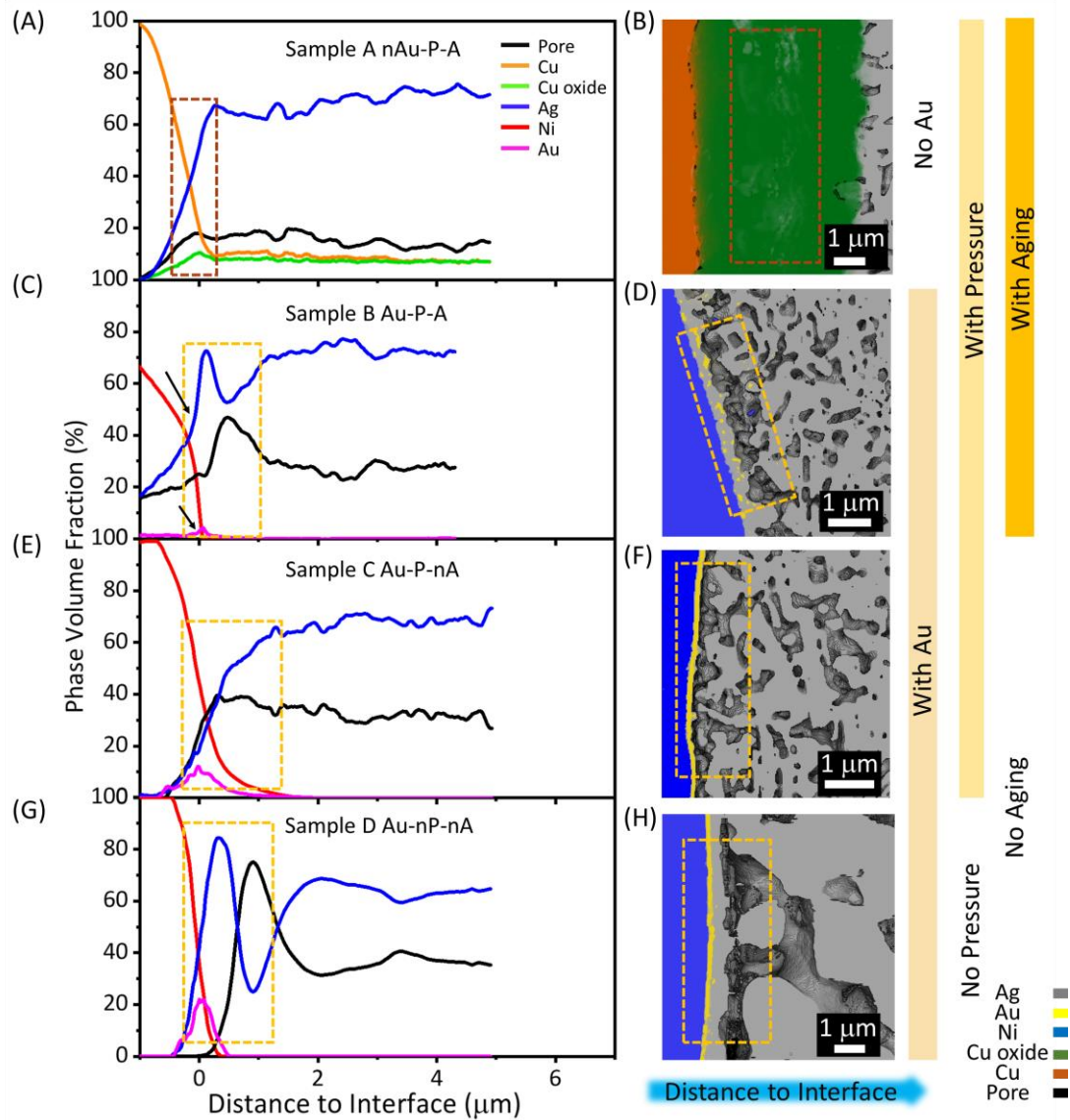
Figure 4 Quantification of phase distribution profiles correlated as a function of die attachment depth with corresponding interface morphology from cross-sectional view of segmented 3D volumes: (A-B) Sample A nAu-P-A, (C-D) Sample B Au-P-A. (E-F) Sample C Au-P-nA. (G-H) Sample D Au-nP-nA. Black arrows in (C) indicate that when Au and Ag layers were directly in contact, the volume fraction of Ag and Au increased together likely due to interdiffusion.
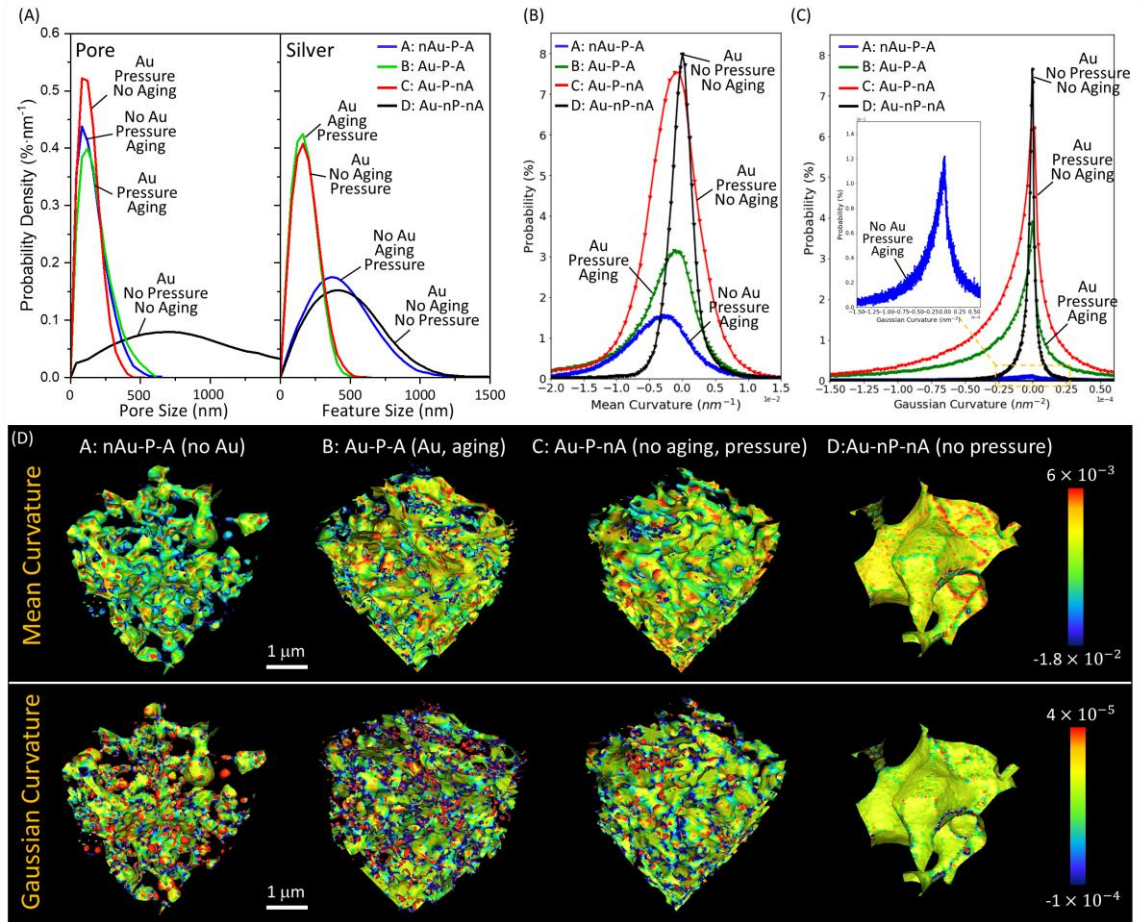
Figure 5 (A) Feature size distribution of Ag and pore size distribution comparison between samples with different control parameters. (B) Histogram of the mean curvature ($H = (K_1 + K_2)/2$) on Ag phase. (C) Histogram of the Gaussian curvature ($K = K_1 K_2$) on Ag phase. (D) 3D visualization of Gaussian and mean curvature comparison for different control parameters.
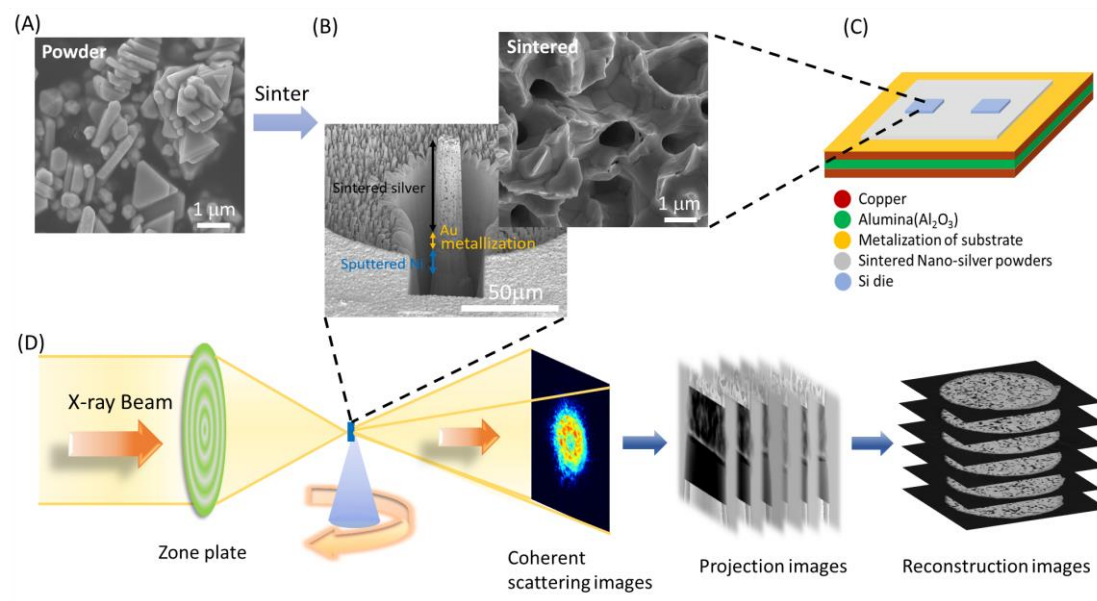
Figure 6 (A) Surface morphology of Ag powder. (B) Left: cross-section profile of sintered Ag porous structure and bonding with Au metallization; right: surface morphology of sintered Ag. (C) Schematic diagram showing the layer structure of sintered Ag. (D) Schematic diagram of ptychographic X-ray computed tomography setup.
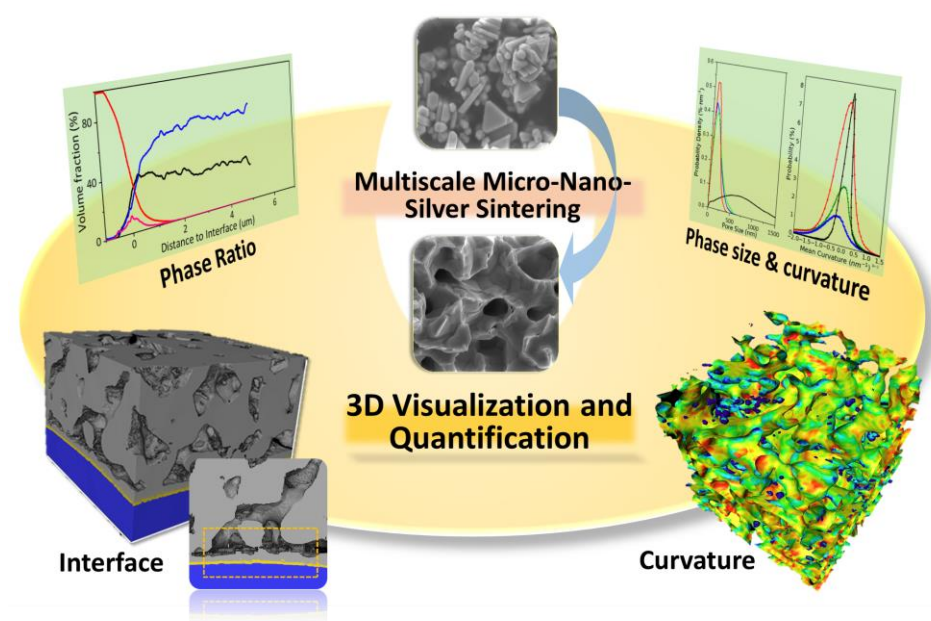
Table of Contents

Supporting Information for:

Unveiling 3D Morphology of Multiscale Micro-Nano Silver Sintering

for Advanced Electronics Manufacturing by Ptychographic

X-ray Nano-Tomography

Yu-Chung Lin[1#], Xiaoyang Liu[1#], Kang-Wei Chou[2], Esther H. R. Tsai[3,5], Chonghang Zhao[1], Mirko Holler[3], Ana Diaz[3], Stanislas Petrash*[2], Yu-chen Karen Chen-Wiegart*[1, 4]

1 Department of Materials Science and Chemical Engineering, Stony Brook University, Stony Brook, NY, 11794, USA
2 Henkel Corporation, Bridgewater, NJ, 08807, USA
3 Paul Scherrer Institut, Forschungsstrasse 111, CH-5232 Villigen, Switzerland
4 National Synchrotron Light Source - II, Brookhaven National Laboratory, Upton, NY, 11973, USA
5 Center for Functional Nanomaterials, Brookhaven National Laboratory, Upton, NY 11973, USA

*Corresponding Authors: karen.chen-wiegart@stonybrook.edu;
stan.petrash@henkel.com
[#] Joint first authors

Experimental Method

1.1 Sample preparation

With pressure-assisted sintering (Samples A-C), the specimen was placed on the hot plate at 130 °C for 12 min. Afterwards, the sample was sintered under a 10 MPa pressure and the temperature was ramped to 250 °C in 15 min with a ramping rate of 15 °C/min from room temperature; the samples were sintered for 5 min at 250°C. For the sample sintered without pressure-assistance (Sample D), the specimen was annealed also by ramping the temperature in 15 min from room temperature to 250°C. However, sintering without pressure requires a longer time, i.e. 60 min. After the sintering process is completed, two of the samples were aged under accelerated condition at 250 °C in air for 24 hours to test their durability. The samples were noted as gold (Au) vs. nAu (no Au) for testing metallization effects, P vs. nP (no pressure) for testing sintering conditions, and A vs. nA for testing the aging effects.

The pristine nano-silver (Ag) powders and the sintered nano-Ag structure are shown in Figure 6 B. The pristine nano-Ag powders are triangle in shape, with ~100 nm thickness and ~2 μm length. The shape is consistent with crystalline Ag nanoparticles[1]. To disperse the Ag nanoparticles, fatty acid was added as a dispersion agent. After sintering, the Ag powders became well-connected, forming a porous structure.

To prepare the samples for the PXCT study, the samples were milled into a cylinder with diameter 14-16 μm by FIB and then lifted-out and mounted to a sample pin specifically developed for the nanoscale scanning instrument used for PXCT [2] measurements following a procedure developed previously [3]. Figure. 6 C shows the sample preparation process after milling by FIB.

1.2 X-ray nano-tomography by ptychography and X-ray fluorescence microscopy

Ptychography [4] is a lensless coherent diffractive imaging method that, when combined with tomography, offers quantitative electron density and absorption tomograms with nanoscopic resolution [5, 6]. In this work, four tomograms were obtained through PXCT experiments carried out at the cSAXS beamline (X12SA) at the Swiss Light Source, Paul Scherrer Institute (PSI), Switzerland. A general description of each tomographic measurement is given as follows. Measurements were conducted in air and at room

temperature with an instrument that allows scanning nano-tomography with about 10 nm position accuracy, well suited for PXCT [8,9]. The experimental setup is illustrated in Figure 6 D.

A double crystal Si (111) monochromator was used to provide a monochromatic radiation of 8.7 keV. The illumination was defined by a 50 μm-diameter central stop, a 170 μm-diameter Fresnel zone plate (FZP) [7] with an outer zone width of 60 nm, and a 30 μm-diameter order sorting aperture. The FZP and the central stop were both fabricated at the Laboratory for Micro and Nanotechnology, PSI, Switzerland. The focal distance was 71 mm and the sample was placed a few millimeters downstream the focus to give an illumination of around 5 μm in diameter. The scanning points followed a Fermat spiral pattern[8] with an average step size of 0.6 μm over a field of view (FOV) of approximately 20 μm horizontally by 10 μm vertically. At each scanning position, a diffraction pattern was collected at 7.3 m downstream of the sample with an exposure time of 0.1 sec using a Pilatus 2M detector [9]. The number of photons incident on a sample was around 7×10^7 photons/μm^2 per projection.

Around 600 projections were taken from 0 to 180 with an angular step of 0.3 , taking approximately 18 hours per tomogram. Ptychographic reconstruction algorithms, including difference map [10] and maximum likelihood [11], were applied to reconstruct 2D projections. Areas of 300 × 300 pixels were used on the detector, giving reconstructed images with a pixel size of about 20 nm. Two-dimensional projections were aligned [12] to give 3D tomograms based on modified filtered back projection. The phase tomograms are quantitative and correspond to the electron density, as shown in Figure S1 [6]. Image resolution was estimated by Fourier shell correlation (FSC) [13] to be around 32 nm.

To examine the elemental composition, simultaneous ptychography and fluorescence scans were performed on sample A for a 2D projection. For the fluorescence analysis, a Ketek energy dispersive detector was placed close to the sample at about 90 degrees from the incident X-ray direction. Measurements were taken at 11.2 keV to cover the emission peaks of Au, Ag, and Cu. A FZP with 100 μm diameter was used and the sample-to-FZP distance was adjusted to give a 2-μm-diameter beam. The sample was

scanned by this illumination at a 0.4 µm step following a Cartesian grid and an exposure time of 0.1 sec. The FOV was 7 µm horizontally and 20 µm vertically. The Ag fluorescence image in Figure 2 was generated by a simple integration of the emission spectra at 2.998 keV with a width of around +/-0.25keV, corresponding to the Lα peak positions. The Cu fluorescence map shows the integrated intensity at 7.998 keV with a width of roughly +/-0.25keV, corresponding to the Kα peaks.
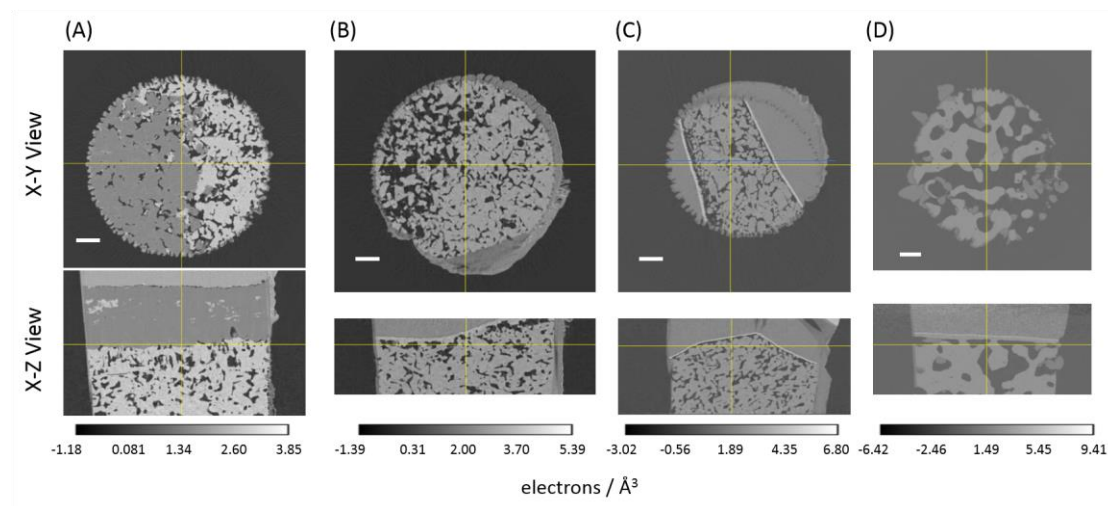

Figure S1 Reconstructed virtual cross section of the four Samples A-D from X-ray ptychographic tomography, with two different orthogonal views. Scale bars indicate 2 µm. Horizontal and vertical lines indicate the same planes for X-Y and XZ views.

1.3 Adhesion Performance Test

Evaluation of adhesion performance was conducted by performing 90° peel test using a peel test device from Frolyt GmbH (Freiberg, Germany). A peel speed of 8 mm/sec was used for all samples.

1.4 Three-dimensional morphological analysis

Quantitative morphology studies were performed directly on the measured 3D datasets, as has been previously done in other tomography studies using a transmission X-ray microscope [14]. In the following we describe the different aspects of this analysis in detail.

1.4.1 Segmentation

The central region in each of the 3D reconstruction image stack was cropped for further analysis. PXCT provides tomograms in which voxels have quantitative values of the

electron density of the sample, which for many light elements can be accurately converted to mass density [6]. Therefore, different materials in the sample can be segmented by their different densities and can be sometimes identified by their density values. The segmentation was conducted using Avizo software (FEI, Ver. 9.4). The phases including Cu, Cu oxide, Ni, Ag, Au and pore (air) were segmented directly using thresholding as their corresponding peaks in the histogram are well separated. For sample B (Au-P-A), as the Ag and Au peaks in the histogram overlap, the threshold value between Ag and Au phases was determined within a range where the slope of the histogram changes, indicating the mid-range of two overlapping peaks; while this process was semi-quantitative, within this range the morphological quantitative analysis results remain similar as the amount of Au is low. After the threshold value was determined, the artifacts of the threshold segmentation were examined by comparing the segmented images with the raw images and the segmented areas were corrected in Avizo. The 3D volume rendering was then conducted, and the segmented data were used for further 3D morphological quantification.

1.4.2 Phase distribution profile and feature size distribution

The various 3D morphological parameters were quantified using customized Matlab code developed in-house at Stony Brook University and Brookhaven National Laboratory. The phase distribution profiles of all phases were determined along the direction that is perpendicular to the interfaces. The distance was measured relative to the Ag-metal interface, which is defined as the zero position. The volume fraction of each phase at a given 2D plane was determined by voxel counting. The interface location was determined from the peak location of the first derivative of the Ag distribution profile. The feature size distribution of pore and Ag were obtained by well-established methods in the literature [15].

Average, standard deviation and full width half maximum (FWHM) of mean curvature of samples made at different conditions

Sample	Average (nm^{-1})	Median (nm^{-1})	Standard Deviation (nm^{-1})	FWHM (nm^{-1})
A: nAu-P-A	-0.00437	-0.05819	0.00649	0.01014
B: Au-P-A	-0.00461	-0.07517	0.00889	0.00789
C: Au-P-nA	-0.00245	-7E-07	0.00701	0.00822
D: Au-nP-nA	-3.5E-05	0.00314	0.00450	0.00355

Table S1 Average, standard deviation and full width half maximum (FWHM) of mean curvature of samples made at different conditions.

Reference

[1] S. H. Chen, D. L. Carroll, Nano Lett. **2002**, *2*, 1003.

[2] M. Holler, J. Raabe, R. Wepf, S. H. Shahmoradian, A. Diaz, B. Sarafimov, T.

Lachat, H. Walther, M. Vitins, Rev. Sci. Instrum. **2017**, *88*, 113701.

[3] Y. C. K. Chen-Wiegart, F. E. Camino, J. Wang, ChemPhysChem **2014**, *15*,

1587.

[4] J. M. Rodenburg, A. C. Hurst, A. G. Cullis, B. R. Dobson, F. Pfeiffer, O. Bunk, C.

David, K. Jefimovs, I. Johnson, Phys. Rev. Lett. **2007**, *98*, 034801; H. M. L.

Faulkner, J. M. Rodenburg, Phys. Rev. Lett. **2004**, *93*, 4.

[5] M. Holler, M. Guizar-Sicairos, E. H. R. Tsai, R. Dinapoli, E. Muller, O. Bunk, J.

Raabe, G. Aeppli, Nature **2017**, *543*, 402; M. Dierolf, A. Menzel, P. Thibault, P.

Schneider, C. M. Kewish, R. Wepf, O. Bunk, F. Pfeiffer, Nature **2010**, *467*, 436.

[6] A. Diaz, P. Trtik, M. Guizar-Sicairos, A. Menzel, P. Thibault, O. Bunk, Phys.

Rev. B **2012**, *85*, 020104(R).

[7] S. Gorelick, J. Vila-Comamala, V. A. Guzenko, R. Barrett, M. Salome, C. David,

J. Synchrotron Radiat. 2011, 18, 442.

[8] X. J. Huang, H. F. Yan, R. Harder, Y. K. Hwu, I. K. Robinson, Y. S. Chu, Opt.

Express **2014**, *22*, 12634.

[9] B. Henrich, A. Bergamaschi, C. Broennimann, R. Dinapoli, E. F. Eikenberry, I.

Johnson, M. Kobas, P. Kraft, A. Mozzanica, B. Schmitt, Nucl. Instrum. Methods

Phys. Res., Sect. A **2009**, *607*, 247.

[10] P. Thibault, M. Dierolf, A. Menzel, O. Bunk, C. David, F. Pfeiffer, Science **2008**,

321, 379.

[11] M. Guizar-Sicairos, J. R. Fienup, Opt. Express **2008**, *16*, 7264; P. Thibault, M. Guizar-Sicairos, New J. Phys. **2012**, *14*, 063004.

[12] M. Guizar-Sicairos, A. Diaz, M. Holler, M. S. Lucas, A. Menzel, R. A. Wepf, O. Bunk, Opt. Express **2011**, *19*, 21345; M. Guizar-Sicairos, J. J. Boon, K. Mader, A. Diaz, A. Menzel, O. Bunk, Optica **2015**, *2*, 259.

[13] M. van Heel, M. Schatz, J. Struct. Biol. **2005**, *151*, 250.

[14] Y. C. K. Chen-Wiegart, P. Shearing, Q. X. Yuan, A. Tkachuk, J. Wang, Electrochem. Commun. **2012**, *21*, 58; Y. C. K. Chen-Wiegart, T. Wada, N. Butakov, X. H. Xiao, F. De Carlo, H. Kato, J. Wang, D. C. Dunand, E. Maire, J. Mater. Res. **2013**, *28*, 2444; Y. C. K. Chen-Wiegart, J. S. Cronin, Q. X. Yuan, K. J. Yakal-Kremski, S. A. Barnett, J. Wang, J. Power Sources **2012**, *218*, 348; Y. J. Liu, F. Meirer, C. M. Krest, S. Webb, B. M. Weckhuysen, Nat. Commun. **2016**, *7*; Y. C. K. Chen, Y. S. Chu, J. Yi, I. McNulty, Q. Shen, P. W. Voorhees, D. C. Dunand, Appl. Phys. Lett. **2010**, *96*; Y. J. Liu, F. Meirer, J. Y. Wang, G. Requena, P. Williams, J. Nelson, A. Mehta, J. C. Andrews, P. Pianetta, Anal. Bioanal. Chem. **2012**, *404*, 1297; G. J. Nelson, W. M. Harris, J. J. Lombardo, J. R. Izzo, W. K. S. Chiu, P. Tanasini, M. Cantoni, J. Van Herle, C. Comninellis, J. C. Andrews, Y. J. Liu, P. Pianetta, Y. S. Chu, Electrochem. Commun. **2011**, *13*, 586.

[15] J. Alkemper, P. W. Voorhees, Acta Mater. **2001**, *49*, 897; B. Munch, L. Holzer, J. Am. Ceram. Soc. **2008**, *91*, 4059; Y. C. K. Chen-Wiegart, S. Wang, Y. S. Chu, W. J. Liu, I. McNulty, P. W. Voorhees, D. C. Dunand, Acta Mater. **2012**, *60*, 4972.